batteries

MDPI

Article

Titanium Activation in Prussian Blue Based Electrodes for Na-ion Batteries: A Synthesis and Electrochemical Study

Min Li [1], Angelo Mullaliu [2,3], Stefano Passerini [2,3] and Marco Giorgetti [1,*]

[1] Department of Industrial Chemistry "Toso Montanari", University of Bologna, Viale Risorgimento 4, 40136 Bologna, Italy; min.li2@unibo.it
[2] Helmholtz Institute Ulm (HIU), Helmholtzstrasse 11, 89081 Ulm, Germany; angelo.mullaliu@kit.edu (A.M.); stefano.passerini@kit.edu (S.P.)
[3] Karlsruhe Institute of Technology (KIT), P.O. Box 3640, 76021 Karlsruhe, Germany
* Correspondence: marco.giorgetti@unibo.it

Abstract: Sodium titanium hexacyanoferrate (TiHCF, $Na_{0.86}Ti_{0.73}[Fe(CN)_6]\cdot 3H_2O$) is synthesized by a simple co-precipitation method in this study. Its crystal structure, chemical composition, and geometric/electronic structural information are investigated by X-ray powder diffraction (XRPD), microwave plasma-atomic emission spectroscopy (MP-AES), and X-ray absorption spectroscopy (XAS). The electroactivity of TiHCF as a host for Li-ion and Na-ion batteries is studied in organic electrolytes. The results demonstrate that TiHCF is a good positive electrode material for both Li-ion and Na-ion batteries. Surprisingly, however, the material shows better electrochemical performance as a Na-ion host, offering a capacity of 74 mAh g^{-1} at C/20 and a 94.5% retention after 50 cycles. This is due to the activation of Ti towards the redox reaction, making TiHCF a good candidate electrode material for Na-ion batteries.

Keywords: titanium hexacyanoferrate; cathode material; Na/Li-ion batteries

Citation: Li, M.; Mullaliu, A.; Passerini, S.; Giorgetti, M. Titanium Activation in Prussian Blue Based Electrodes for Na-ion Batteries: A Synthesis and Electrochemical Study. *Batteries* **2021**, *7*, 5. https://doi.org/10.3390/batteries7010005

Received: 28 November 2020
Accepted: 5 January 2021
Published: 7 January 2021

1. Introduction

After the first report of Vernon D. Neff [1] in 1978 reporting the electrochemical activity of Prussian blue (PB; with the generic formula $A_xFe[Fe(CN)_6]$, where A stands for an alkali metal), PB and Prussian blue analogs (PBAs; $A_xM[M'(CN)_6]$, M and M′ = transition metals) have been widely studied in electrochromism [2,3], electrocatalysis [4,5], potentiometric and amperometric sensors [6,7], and more recently, as electrode materials in electrochemical energy storage systems [8–15]. PBAs can be considered as bimetallic cyanides, where the structural unit NC-M′-CN-M-NC- repeats in cubic lattice in most of the analog. M and M′ sites are sixfold coordinated, with the former to the nitrogen atoms of the CN ligands, and the latter octahedrally coordinated to the carbon atoms of the cyanides. Overall, this peculiar structure with 3D framework, contains large ionic channels and interstices, as well as abundant redox-active sites, and is characterized by strong structural stability [16,17]. Benefiting from these structural features, PBAs have been intensively investigated as a new alternative and low-cost host material that can accommodate not only monovalent alkali cations such as Li^+, Na^+, and K^+ ions [8–10], but also divalent and trivalent cations including Mg^{2+}, Zn^{2+}, Ca^{2+}, and Al^{3+} [11–15].

Cui and coworkers [18,19] reported the utilization of copper hexacyanoferrate (CuHCF) and nickel hexacyanoferrate (NiHCF) as cathode materials in aqueous sodium and potassium batteries, which showed excellent cycling performance and rate capability. Moritomo et al. [20] and Goodenough et al. [9] reported the manganese hexacyanoferrate analog (MnHCF) delivering high specific capacity (109 mAh g^{-1} and 143 mAh g^{-1}, respectively), which is close to the theoretical capacity of the well-known $LiMn_2O_4$ (148 mAh g^{-1}) positive electrode material. In addition to MnHCF, PB and cobalt hexacyanoferrate (CoHCF) also displayed

high reversible specific capacities due to the two redox active sites (Fe and Co, respectively) [21–23]. Most hexacyanoferrates exhibit high voltage plateaus; for example, PB displays an average discharge plateau around 3 V vs. Na^+/Na [21,22], CoHCF at 3.6 V vs. Na^+/Na [23], while MnHCF at 3.6 V vs. Li^+/Li and 3.4 V vs. Na^+/Na [24]. The presence of not only high- but also low-voltage plateaus has contributed in the past few years to the development of cathode and anode materials based on PBAs [25]. Indeed, hexacyanomanganates ($AM[Mn(CN)_6]$) [26,27], hexacyanocobaltates ($AM[Co(CN)_6]$) [28], and hexacyanochromates ($AM[Cr(CN)_6]$) [29] are reported as anode materials, displaying high reversible capacity at low potential (1.8 V vs. Na^+/Na and ~1.5 V vs. Li^+/Li in organic electrolyte, −0.86 V vs. SHE(standard hydrogen electrode) in aqueous solution).

Among the several PBA electrode materials, titanium hexacyanoferrate (TiHCF) has aroused our interest because Fe (5.6%) and Ti (0.61%) are in the top 10 most abundant elements within the earth's crust. Their high abundance and correspondingly low cost of raw materials enable them to be potential candidates for future large-scale energy-storage applications. Secondly, Ti-based compounds have been widely investigated as both anode (TiO_2, $Li_4Ti_5O_{12}$, TiS_2, $MLi_2Ti_6O_{14}$, etc.) [30–32] and cathode (Ni/Mn/Fe/Co/Cr-Ti binary/ternary/multinary system) materials [33–36]. The studies about TiHCF in electrochemical applications are very limited, and the reported articles show different results about the electrochemical properties of TiHCF. Chen et al. first reported the anode properties of $Ti_{0.75}Fe_{0.25}[Fe(CN)_6]_{0.96}\cdot 1.9H_2O$ for Li-ion and Na-ion batteries, with a discharge potential lower than 1 V [37]. However, Wu et al. [38] and Xu et al. [39] reported that TiHCF showed good electrochemical performance for Na-ion and K-ion batteries as a cathode electrode. These different results stimulated our research interest accordingly. Here in this study, TiHCF containing both titanium (Ti) and iron (Fe) sites is synthesized by a controlled co-precipitation method, and its electrochemical properties as an electrode material are explored as both Li-ion and Na-ion electrode materials in organic electrolytes.

2. Results

2.1. Preparation and Characterization of TiHCF

TiHCF was synthesized based on a simple and reproducible co-precipitation method. The stoichiometry of the resulting TiHCF material is $Na_{0.86}Ti_{0.73}[Fe(CN)_6]\cdot 3H_2O$ after a microwave plasma-atomic emission spectroscopy (MP-AES) composition analysis and thermogravimetric (TG) analysis, which show two distinct weight-loss events, as displayed in Figure 1a. The weight loss below 120 °C corresponds to the loss of adsorbed water, while the one between 120–200 °C can be assigned to the elimination of interstitial water [40]. In our sample, the total water content is about 17.7%, with around 8.4% adsorbed water and 9.3% interstitial water.

The X-ray powder diffraction (XRPD) pattern of the as-synthesized sample and its refinement are shown in Figure 1b. TiHCF powder displayed a low degree of crystallinity. The refinement is consistent with a cubic structure (space group: Pm-3m) with a quotation of a lattice parameter of 9.862(5) Å. The size and morphology of the TiHCF sample are shown in Figure S1; it consists of variously shaped particles with an average diameter of around 50 nm. IR spectroscopy of TiHCF is shown in Figure 1c. A broad peak occurs around 3000–3600 cm^{-1}, which can be attributed to the stretching mode of -O-H groups from the absorbed and coordinated water. Meanwhile, the peak at 1610 cm^{-1} is related to the bending mode of -O-H group. Two distinguishable peaks appeared at around 2077 cm^{-1} and 2010 cm^{-1}, which are characteristic of the -C≡N group. The value of the -C≡N ligand stretching is highly sensitive to the different chemical environment surrounding the functional group as well as the bond strength. In this case, the vibration band at 2077 cm^{-1} is associated with Ti^{IV}-N≡C-Fe^{II}. This is consistent with the ferrocyanide precursor, while the small peak located at 2010 cm^{-1} is due to terminal nonbridging cyanides [41,42].

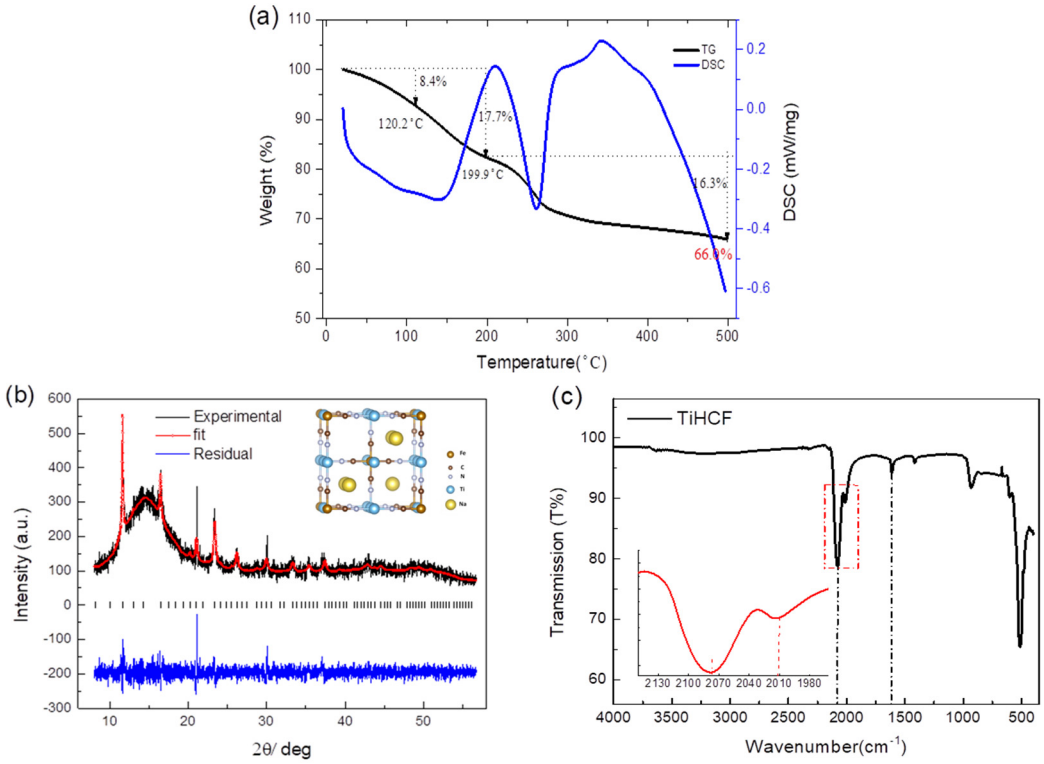

Figure 1. (**a**) Thermogravimetric analysis (TGA) of TiHCF powder and the crystal structure model (inside); (**b**) X-ray powder diffraction (XRPD) pattern and Rietveld refinement on TiHCF powder. The broad peak at around 10–17 degrees is due to the capillary sample holder; (**c**) infrared transmission spectrum of TiHCF powder.

X-ray absorption spectroscopy (XAS) is a widely used technique for determining the local geometric and/or electronic structure of the absorbing atom. Figure 2a displays the titanium K-edge spectrum regions—i.e., the pre-edge (labeled as A), a feature B in the rising portion of the X-ray absorption near edge structure (XANES), and the EXAFS region (extended X-ray absorption fine structure), indicated as C. Absorption in the pre-edge region is due to transitions of 1 s core electrons to bound excited electronic states, providing a wealth of structural and electronic information. As shown in Figure 2b, one appreciable peak at around 4970.9 eV and one broad peak at around 4974.5 eV are present. Howe et al. [43] reported three pre-edge peaks in anatase (TiO_2) Ti K-edge and labeled them as A1 (4968.8 eV), A3 (4971.9 eV), and B (4974.3 eV); Kuroda et al. [44] and Kotani et al. [45] also reported the A1, A2, and B peaks in the rutile and anatase Ti K-edge. Even though there is some disagreement in the value of the absolute edge energies, there is a general consensus that all A and B transitions are due to dipole forbidden transitions of the core electrons to 3d-4p hybridized states. Given that the intensity of the pre-edge transition is sensitive to the symmetry of the surrounding atoms and that here, Ti is coordinated to 6 nitrogen atoms, the appearance and the relatively high intensity of the pre-edge peaks indicate distortion from the Oh symmetry.

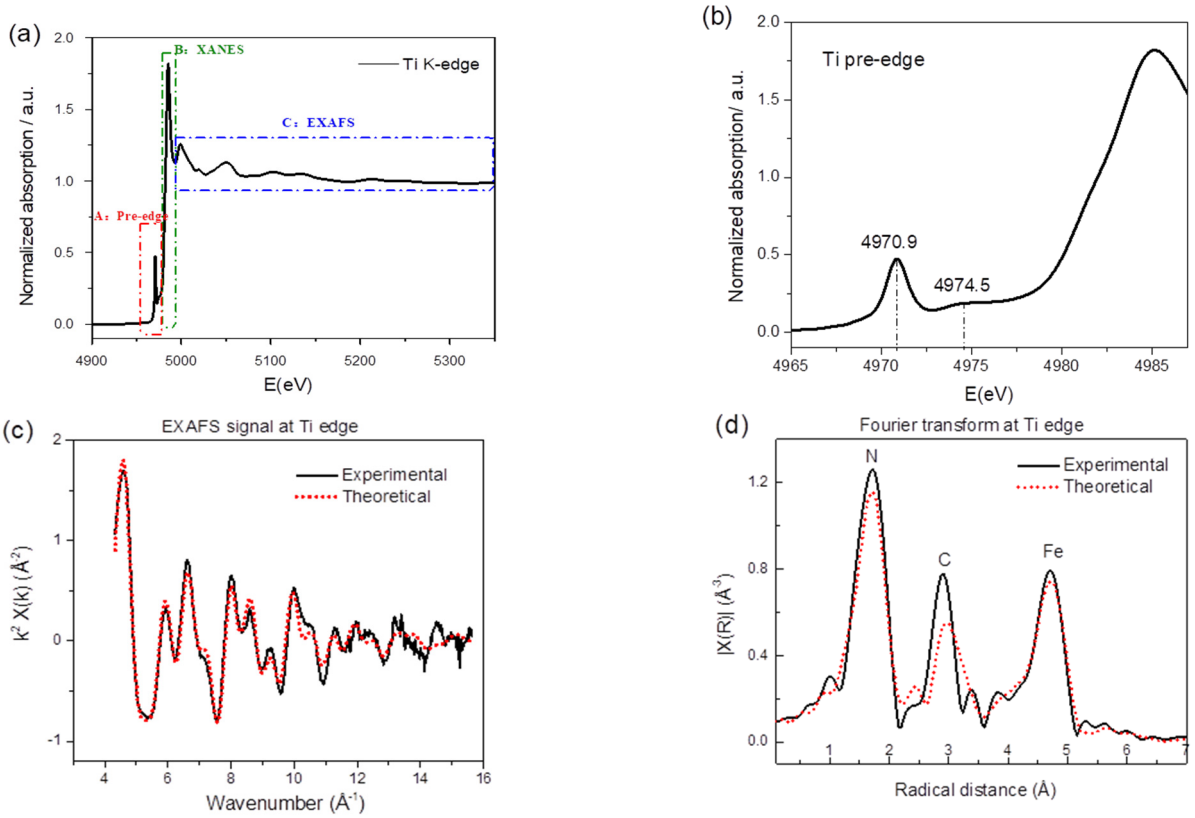

Figure 2. (**a**) Normalized X-ray absorption spectrum of TiHCF powder at the titanium K-edge. (**b**) Zoom-in of the pre-edge feature of Ti K-edge. (**c**) Comparison of the experimental and theoretical k^2-extracted EXAFS (extended X-ray absorption fine structure) signal and (**d**) corresponding Fourier transform (FT).

Due to the strong selectivity of the XAS probe, additional local structural information around the titanium can be gained by analyzing the extended portion of the XAS spectrum, i.e., the EXAFS. Figure 2c reports the comparison of the theoretical and experimental EXAFS signal while the panel in Figure 2d shows the corresponding Fourier transform (FT). The theoretical curve matches well in both panels, testifying the quality of the present data analysis. The EXAFS signal is well structured and is most likely composed of several sinusoidal contributions. This becomes evident from the FT curve, as it displays three shells of scattering atoms around the Ti. According to the TiHCF framework structure, the position of the first peak is attributed to Ti-N, while the second and third peaks are attributed to the carbon (Ti-N-C) and iron (Ti-N-C-Fe). Details of the fitting procedure are shown in Figure S1. From the best-fit, the Fe-C, C-N, and Ti-N bond lengths were found to be 1.87(2), 1.18(2), and 2.07(9) Å, respectively. The values for Fe-C and C-N are consistent with the one reported for this class of compounds [17,24]; the Ti-N is similar to the metal linked to the N end of the cyanide group in iron hexacyanocobaltate [46] and in agreement with the quotation of the Ti-N first shell in titanium nitride (octahedral coordination for Ti) [47].

2.2. Electrochemical Application of TiHCF

The electrochemical performance of TiHCF electrodes was tested in an organic electrolyte against either Na or Li in a coin cell assembly. The cyclic voltammetry (CV) curves of the Na and Li coin cells at different scan rate values are shown in Figure 3a,b. When tested at a high scan rate, only one pair of redox peaks appeared, at around 3.0/3.9 V vs. Na^+/Na and 3.4/3.7 V vs. Li^+/Li. By testing the cell at a lower scan rate, for instance, at 0.2 mV s^{-1}, an additional pair of reversible peaks appeared around 2.6 V and 3.5 V vs. Na^+/Na and 2.8 V and 3.7 V vs. Li^+/Li, as shown in Figure 3c,d. Wu et al. [38] and Xu et al. [39] reported the CV curves of sodium/potassium TiHCF featuring two main

characteristic pairs of peaks: one at about 3.0/2.6 V due to the $Ti^{4+/3+}$ couple, the other at 3.4/3.2 V which was assigned to the $[Fe\ (CN)_6]^{4-/3-}$ couple. Thus, based on these works, the redox peak at 2.6/2.8 V is attributed to the Ti^{4+}/Ti^{3+}, and the redox peak around 3.5/3.6 V is ascribed to the Fe^{3+}/Fe^{2+} pair. Overall, the electrochemical discharge reaction can be described as:

$$Na(Li)_x Ti^{IV}_{0.73}\left[Fe^{III}(CN)_6\right] + Li^+(Na^+)_y + ye^- \leftrightharpoons Na(Li)_{x+y} Ti^{IV}_{0.73}\left[Fe^{II}(CN)_6\right] \quad (1)$$

$$Na(Li)_x Ti^{IV}_{0.73}\left[Fe^{II}(CN)_6\right] + Li^+(Na^+)_y + ye^- \leftrightharpoons Na(Li)_{x+y} Ti^{III}_{0.73}\left[Fe^{II}(CN)_6\right] \quad (2)$$

where Equation (1) is relative to the high voltage peaks (3.5 V vs. Na^+/Na or 3.7 vs. Li^+/Li), while Equation (2) is relative to the redox peak at 2.6 V vs. Na^+/Na (or 2.8 vs. Li^+/Li). In the following, we argue that the relative occurrence of the processes described in (1) and (2) will change upon cycling against Na only.

The cycling performance of TiHCF in Na-ion and Li-ion half cells are shown in Figure 4a,b. TiHCF exhibits good capacity retention: 94.5% and 89.9% of the discharge capacity values were retained after 50 cycles in the Na and Li coin cells, respectively. Both cells feature a low coulombic efficiency at the beginning of the cycling, but after roughly 10 cycles, the coulombic efficiency reached and kept at a stable value (96–97%). According to the report of Goodenough et al. [48], the most probable cause for low coulombic efficiency in the first cycles is related to the structural water inside the compound. Briefly, the water molecules adsorbed in the interstices of the PBA framework may decompose during charge, causing a low efficiency. With subsequent cycling, the amount of residual water would decrease, and the efficiency is restored to a stable value. A similar behavior has also been reported for another Prussian blue-like electrode, namely the iron hexacyanocobaltate [46].

Figure 4c,d displays the galvanostatic charge/discharge profiles of the Na and Li coin cells at C/20, respectively. For the Na coin cell, two sloping discharge plateaus centered at 3.5 and 2.6 V were observed, which are consistent with the two redox peaks observed in the CV curve (cf. Figure 3c). The overall discharge capacity in the first cycle is around 74 mAh g^{-1}. By considering 1 mol of Na^+ participating in the reaction, the calculated theoretical capacity of TiHCF ($Na_{0.86}Ti_{0.73}[Fe\ (CN)_6]\cdot 3H_2O$) is 83.6 mAh g^{-1}. However, our TiHCF contains only 0.86 mol Na^+ and the corresponding capacity should be $0.86 \times 83.6 = 71.9$ mAh g^{-1}, which is consistent with the stable value obtained upon cycling. Therefore, this indicates that during the charge and discharge processes, all the available Na^+ ions in the pristine structure participate in the electrochemical reaction. It was not possible, at present, to reversibly intercalate more sodium.

On the other side, for the Li coin cell (cf. Figure 4d), only one sloping discharge plateau was observed, with a lower discharge capacity (40 mAh g^{-1} in the first cycle) compared to the Na coin cell. The difference in the insertion chemistry for the Na^+ vs. Li^+ is relevant, as there are not so many examples in the literature where the same electrode material displays higher performance upon Na storage than Li storage [24]. It is most likely that the Na^+ extraction in the first charge, coming from the sodium inside the pristine structure, does not favor the successive Li^+ ion insertion and release in Li cells. On the contrary, the sodium release/insertion occurs more easily in Na cells.

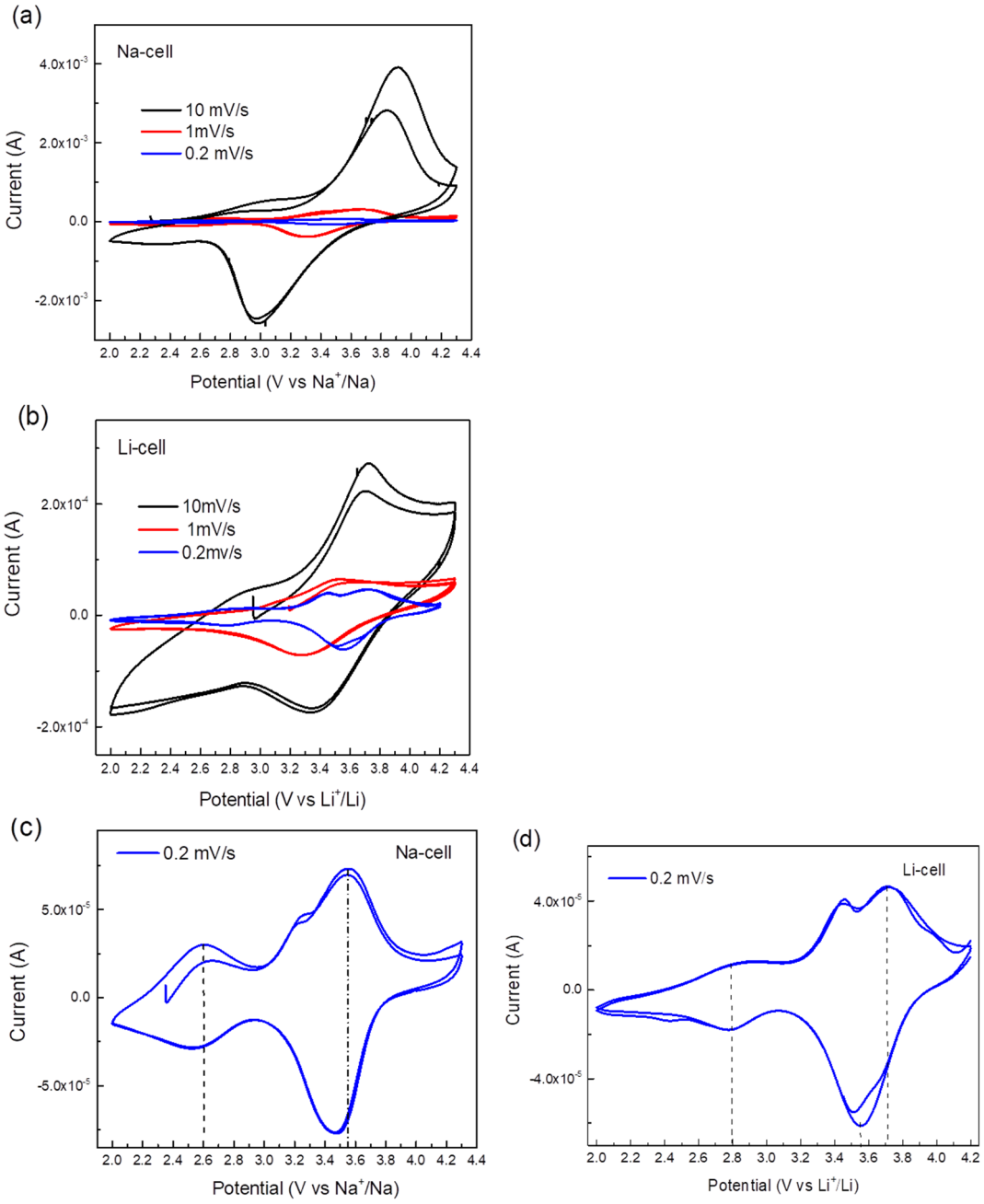

Figure 3. (**a**) Cyclic voltammetry (CV) curves of a TiHCF Na-ion half-cell at a different scan rate (two cycles at each scan rate); (**b**) CV curves of a TiHCF Li-ion half-cell at different scan rate (two cycles at each scan rate); (**c**) CV of TiHCF Na-cell at 0.2 mV/s; (**d**) CV of TiHCF Li-cell at 0.2 mV/s.

To quantify the capacity contribution of the Ti^{4+}/Ti^{3+} and Fe^{3+}/Fe^{2+} redox sites at different voltage ranges, the total discharge capacity during the whole cycling process was divided into three main contributions for the Na-cell (corresponding to the 2.0–3.0 V, 3.0–4.0 V and >4.0 V voltage range) and the Li-cell (corresponding to the 2.3–3.0 V, 3.0–4.0 V and >4.0 V voltage range). The two discharge plateaus centered at 2.6 and 3.5 V are defined to represent the voltage ranges of 2.0–3.0 V and 3.0–4.0 V in the Na-cell, which are ascribed to the Ti^{4+}/Ti^{3+} and Fe^{3+}/Fe^{2+} redox couples, respectively. In the galvanostatic discharge process in the Na-ion electrolyte, the Fe^{3+}/Fe^{2+} reduction contributed to 54.8% of the discharge capacity in the first cycle, while the Ti^{4+}/Ti^{3+} reduction contributed to 45.0%, as shown in Figure 4e. With cycling, the contribution of the Fe^{3+}/Fe^{2+} couple gradually decreased, but the contribution of the Ti^{4+}/Ti^{3+} increased to 63.9% in the 50th cycle. This

suggests that the relative contribution of Equations (1) and (2) changes with cycling and that with the insertion and extraction of Na^+, more Ti sites were activated upon cycling. However, a different situation was found for the Li cell, as shown in Figure 4f. During the cycling, the 3.0–4.0 V voltage range contributes to most of the capacity, providing 77.3% of the total discharge capacity in the first cycle and 76.2% in the 50th cycle, which is mainly attributed to the reduction of Fe^{3+}/Fe^{2+}. The remaining capacity between 2.3–3.0 V is mainly delivered by the Ti^{4+}/Ti^{3+} couple with a constant contribution of 22%. As opposed to the Na case, no increasing activation of the Ti sites was identified during cycling. The difference may be attributable to the different sizes of the Na^+ and Li^+ solvated ions. This can partly explain the higher capacity for Na-ion coin cells, and it also points out the potential application of TiHCF as an electrode material for Na-ion batteries.

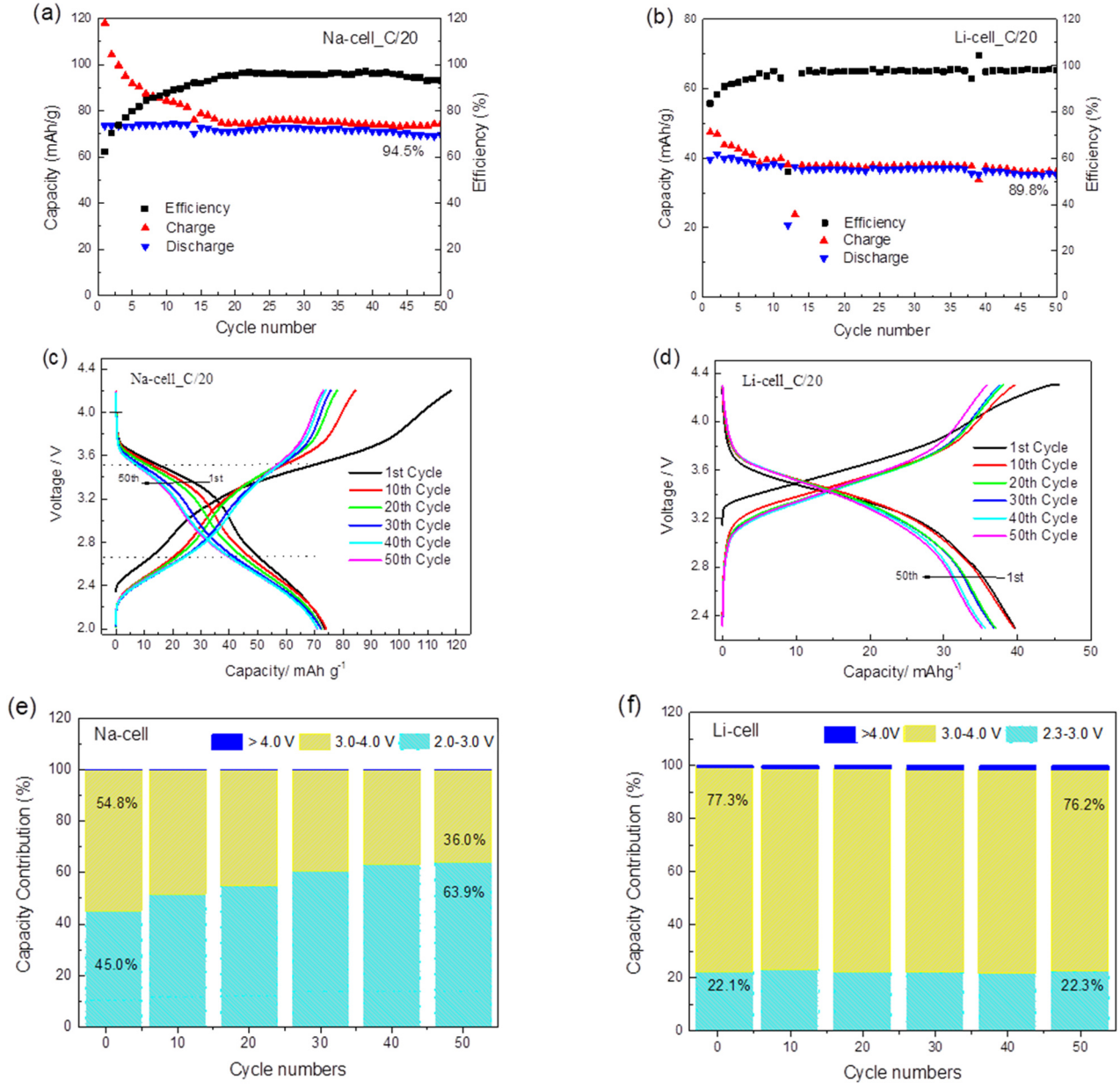

Figure 4. (**a**) Cycling performance of a Na-ion half-cell at C/20 between 2.0–4.2 V; (**b**) cycling performance of a Li-ion half-cell at C/20 between 2.3–4.3 V; (**c**) galvanostatic charge/discharge plot of a Na-ion half-cell at C/20; (**d**) galvanostatic charge/discharge plot of a Li-ion half-cell at C/20; (**e**) the corresponding discharge capacity contribution of different voltage range in a Na-ion half-cell after various cycles at the C/20; (**f**) the corresponding discharge capacity contribution of different voltage range in Li-ion half cell after various cycles at C/20. The applied current densities are 0.0061 mA/cm^2 for Na cell and 0.0056 mA/cm^2 for the Li cell.

3. Materials and Methods

3.1. Material Synthesis

The synthesis of TiHCF was based on a simple and reproducible method, i.e., by mixing tetrabutyl titanate (50 mL 0.1 M, $C_{16}H_{36}O_4Ti$, Sigma Aldrich) ethanol solution with sodium ferrocyanide (100 mL 0.1 M, $Na_4Fe(CN)_6$, Sigma Aldrich) aqueous solution which contains 1.5 M HCl under continuous stirring to generate a precipitate. Because tetrabutyl titanate is easily hydrolyzed, the synthesis was carried out under an inert N_2 atmosphere. After completing the addition of the reagents, the suspension was maintained at 40 °C for another 6 h under N_2 atmosphere and then aged for 4 days at room temperature. The obtained dark-green precipitate was centrifuged and washed with water and acetone, and finally dried in a vacuum oven at 70 °C overnight.

3.2. Electrode Preparation and Electrochemical Tests

For the electrode preparation, the electrode slurry was prepared by mixing 85 wt% of active material, 10 wt% super C65 (IMERYS), and 5 wt% PVDF (polyvinylidene difluoride; Alfa Aesar), which was dissolved (10 wt%) in N-methyl-2-pyrrolidone (NMP). Additional NMP was added to adjust the viscosity of the slurry. The final solid content $m_{solid}/(m_{solid+solvent})$ was 20%. The materials were mixed with a ball milling procedure consisting of 1 h mixing in each direction with a 10 min break in-between stages. The slurry was cast on Al-foil (thickness 20 um, cleaned with ethanol before) using a blade coater (200 µm height), and dried at 60 °C overnight. The disk electrodes have a diameter of 12 mm and a mass loading of around 1.39 (±0.14) mg/cm^2. The electrodes were extensively vacuum-dried at 120 °C and stored in an Ar-filled glove box. Finally, the coin cells were assembled in a 2032 stainless steel coin cell under an inert atmosphere in an Ar-filled glovebox, and Whatman GF/A glass fiber was used as a separator. For Li-ion half-cells, lithium metal foil (thickness 500um, Honjo) was adopted as the negative electrode, and 1 M $LiPF_6$ in a 1:1 ethylene carbonate to dimethyl carbonate volumetric mixture (1EC:1DMC) without additives was used as the electrolyte. For Na-ion half-cells, sodium metal (cut from sodium sticks, Acros Organic, 99.8%) was used as the negative electrode, and $NaPF_6$ in 1 M propylene carbonate (PC) was used as the electrolyte.

Cyclic voltammetry (CV) was performed by means of CHI 660 (CHInstrument, Inc.). The scan was conducted in the potential range of 2.3–4.3 V vs. Li^+/Li or 2.0–4.2 V vs. Na^+/Na. An MTI battery analyzer was employed for galvanostatic cycling, and tests were started after a rest time (6 h) at OCP condition. Cells were tested at room temperature.

3.3. Characterization

Microwave plasma-atomic emission spectrometer (MP-AES) 4210 was used to detect the composition of the active material. During the test, three different wavelengths were chosen for each element.

The infrared (IR) spectrum was collected with a Bruker Alpha FT-IR spectrometer in ATR (attenuated total reflectance) mode in the spectral range of 4000–400 cm^{-1}.

Thermogravimetric analysis (TGA) was performed in air atmosphere from room temperature to 500 °C, with a heating rate of 5 °C min^{-1}, and rapid cooling.

X-ray powder diffraction (XRPD) data were recorded by using a monochromatic X-ray beam (wavelength of 1 Å) at the MCX beamline in Elettra synchrotron Trieste (Italy). Data were collected in a capillary geometry, with the spinner set at 300 rpm. The XRPD pattern was collected consecutively in the range $8° < 2\theta < 56°$, with steps of 0.01°, and an acquisition time of 1 s/step. The profile was refined with a Thompson–Cox–Hastings pseudo-Voigt axial divergence asymmetry peak shape using Fullprof Suite software [49].

X-ray absorption spectroscopy (XAS) experiments were conducted at the Elettra Sincrotrone Trieste (Italy), at the XAFS 11.1 beamline. The storage ring operated at 2.0 GeV in top-up mode with a typical current of 300 mA. Data were recorded at the Ti K-edge in transmission mode using ionization chambers filled with a mixture of Ar, N_2, and He to have 10%, 70%, and 95% of absorption in the I_0, I_1, and I_2 chambers, respectively. An

internal reference of titanium was used for energy calibration in each scan. This allowed for the continuous monitoring of the energy during consecutive scans. The white beam was monochromized using a fixed exit monochromator equipped with a pair of Si (111) crystals. Spectra were collected with a constant k-step of 0.3 nm^{-1} with 3 s per point and acquired from 4880 to 5600 eV (Ti K-edge). XAS spectra were calibrated using the Athena program [50].

4. Conclusions

In this work, TiHCF was synthesized by a simple co-precipitation method and tested in both Na and Li cells employing organic carbonate-based electrolytes. The CV curves of TiHCF in Na and Li cells showed two well-separated peaks centered at 2.6 and 3.5 V vs. Na^+/Na and 2.8 and 3.7 V vs. Li^+/Li, which are ascribable to the $Ti^{4+/3+}$ and $Fe^{3+/2+}$ redox pairs. However, TiHCF displayed a better performance for Na-ion storage electrolyte, showing higher capacity (74 mAh g^{-1} at C/20 rate) and retention (94.5% after 50 cycles), than for Li. This is due to the electrochemical activation of the Ti redox sites in the Na cells, whose contribution to the overall discharge capacity due to the Ti^{IV}/Ti^{III} redox couple gradually increased upon cycling. The results indicate that TiHCF could be a promising candidate for Na-ion batteries; meanwhile, the two well-separated Fe^{3+}/Fe^{2+} and Ti^{4+}/Ti^{3+} redox peaks may enable TiHCF to be used as a bipolar electrode material for Na-ion batteries.

Supplementary Materials: The following are available online at https://www.mdpi.com/2313-0105/7/1/5/s1, Figure S1: Details of the EXAFS analysis of the Ti K-edge of TiHCF in terms of single two-body, three-body, and four-body contribution.

Author Contributions: Preparation, characterization, data analysis, and writing of the original draft, M.L.; conceptualization, supervision, and methodology, M.G.; preparation coin cell, A.M.; EXAFS data analysis, M.G.; writing—review and editing, A.M., S.P., and M.G.; project administration, M.G.; funding acquisition, S.P. and M.G. All authors have read and agreed to the published version of the manuscript.

Funding: This research was funded by the University of Bologna (RFO) and by Sincrotrone ELETTRA through project no. 20165434. The HIU authors acknowledge the basic funding of the Helmholtz Association. This research was also funded by the Italian Ministry of Research (MIUR) within PRIN-2015 Project no. NEWLI2015CL3APH.

Institutional Review Board Statement: Not applicable.

Informed Consent Statement: Not applicable.

Data Availability Statement: Not applicable.

Acknowledgments: The authors thank G. Aquilanti and J. R. Plaisier for their support during the XAS and XRD data acquisition. The Advanced Spectroscopy in Chemistry (ASC) European Joint Master Programme is also acknowledged for enabling international cooperation and financing the study of Min Li.

Conflicts of Interest: The authors declare no conflict of interest.

References

1. Neff, V.D. Electrochemical oxidation and reduction of thin films of Prussian blue. *J. Electrochem. Soc.* **1978**, *125*, 886. [CrossRef]
2. Carpenter, M.K.; Conell, R.S.; Simko, S.J. Electrochemistry and electrochromism of vanadium hexacyanoferrate. *Inorg. Chem.* **1990**, *29*, 845–850. [CrossRef]
3. Kulesza, P.J.; Malik, M.A.; Zamponi, S.; Berrettoni, M.; Marassi, R. Electrolyte-cation-dependent coloring, electrochromism and thermochromism of cobalt (II) hexacyanoferrate (III, II) films. *J. Electroanal. Chem.* **1995**, *397*, 287–292. [CrossRef]
4. Zhou, D.M.; Ju, H.X.; Chen, H.Y. Catalytic oxidation of dopamine at a microdisk platinum electrode modified by electrodeposition of nickel hexacyanoferrate and Nafion. *J. Electroanal. Chem.* **1996**, *408*, 219–223. [CrossRef]
5. Chen, S.M. Characterization and electrocatalytic properties of cobalt hexacyanoferrate. *Electrochim. Acta* **1998**, *43*, 3359–3369. [CrossRef]

6. Eftekhari, A. Aluminum electrode modified with manganese hexacyanoferrate as a chemical sensor for hydrogen peroxide. *Talanta* **2001**, *55*, 395–402. [CrossRef]
7. Garcıa, T.; Casero, E.; Lorenzo, E.; Pariente, F. Electrochemical sensor for sulfite determination based on iron hexacyanoferrate film modified electrodes. *Sens. Actuators B* **2005**, *106*, 803–809. [CrossRef]
8. Matsuda, T.; Moritomo, Y. Thin Film Electrode of Prussian Blue Analogue for Li-ion Battery. *Appl. Phys. Express* **2011**, *4*, 047101. [CrossRef]
9. Wang, L.; Lu, Y.; Liu, J.; Xu, M.; Cheng, J.; Zhang, D.; Goodenough, J.B. A Superior Low-Cost Cathode for a Na-Ion Battery. *Angew. Chem. Int. Ed.* **2013**, *52*, 1964. [CrossRef]
10. Eftekhari, A. Potassium secondary cell based on Prussian blue cathode. *J. Power Sources* **2004**, *126*, 221–228. [CrossRef]
11. Mizuno, Y.; Okubo, M.; Hosono, E.; Kudo, T.; Ohishi, K.; Okazawa, A.; Kojima, N.; Kurono, R.; Nishimura, S.; Yamada, A. Electrochemical Mg^{2+} intercalation into a bimetallic CuFe Prussian blue analog in aqueous electrolytes. *J. Mater. Chem. A* **2013**, *1*, 13055–13059. [CrossRef]
12. Trcoli, R.; La Mantia, F. An Aqueous Zinc-Ion Battery Based on Copper Hexacyanoferrate. *ChemSusChem* **2015**, *8*, 481–485. [CrossRef] [PubMed]
13. Liu, S.; Pan, G.L.; Li, G.R.; Gao, X.P. Copper hexacyanoferrate nanoparticles as cathode material for aqueous Al-ion batteries. *J. Mater. Chem. A* **2015**, *3*, 959. [CrossRef]
14. Kuperman, N.; Padigi, P.; Goncher, G.; Evans, D.; Thiebes, J.; Solanki, R. High performance Prussian blue cathode fornonaqueous Ca-ion intercalation battery. *J. Power Sources* **2017**, *342*, 414–418. [CrossRef]
15. Hu, Y.X.; Ye, D.L.; Hu, B.H.; Zhu, X.B.; Wang, S.C.; Li, L.L.; Peng, S.J.; Wang, L.Z. A binder-free and free-standing cobalt Sulfide@Carbon nanotube cathode material for aluminum-ion batteries. *Adv. Mater.* **2018**, *30*, 1703824. [CrossRef] [PubMed]
16. Keggins, J.F.; Miles, F.D. Structures and Formulæ of the Prussian Blues and Related Compounds. *Nature* **1936**, *137*, 577–578. [CrossRef]
17. Giorgetti, M.; Guadagnini, L.; Tonelli, D.; Minicucci, M.; Aquilanti, G. Structural characterization of electrodeposited copper hexacyanoferrate films by using a spectroscopic multi-technique approach. *Phys. Chem. Chem. Phys.* **2012**, *14*, 5527–5537. [CrossRef]
18. Wessells, C.D.; Peddada, S.V.; Huggins, R.A.; Cui, Y. Nickel Hexacyanoferrate Nanoparticle Electrodes for Aqueous Sodium and Potassium Ion Batteries. *Nano Lett.* **2011**, *11*, 5421–5425. [CrossRef]
19. Wessells, C.D.; Huggins, R.A.; Cui, Y. Copper hexacyanoferrate battery electrodes with long cycle life and high power. *Nat. Commun.* **2011**, *2*, 550. [CrossRef]
20. Matsuda, T.; Takachi, M.; Moritomo, Y. A sodium manganese ferrocyanide thin film for Na-ion batteries. *Chem. Commun.* **2013**, *49*, 2750. [CrossRef]
21. Wang, L.; Song, J.; Qiao, R.M.; Wray, L.A.; Hossain, M.A.; Chuang, Y.D.; Yang, W.L.; Lu, Y.H.; Evans, D.; Lee, J.J.; et al. Rhombohedral Prussian White as Cathode for Rechargeable Sodium-Ion Batteries. *J. Am. Chem. Soc.* **2015**, *137*, 2548–2554. [CrossRef] [PubMed]
22. You, Y.; Yu, X.Q.; Yin, Y.X.; Nam, K.W.; Guo, Y.G. Sodium iron hexacyanoferrate with high Na content as a Na-rich cathode material for Na-ion batteries. *Nano Res.* **2015**, *8*, 117. [CrossRef]
23. Takachi, M.; Matsuda, T.; Moritomo, Y. Cobalt Hexacyanoferrate as Cathode Material for Na^+ Secondary Battery. *Appl. Phys. Express* **2013**, *6*, 025802. [CrossRef]
24. Mullaliu, A.; Asenbauer, J.; Aquilanti, G.; Passerini, S.; Giorgetti, M. Highlighting the Reversible Manganese Electroactivity in Na-Rich Manganese Hexacyanoferrate Material for Li- and Na-Ion Storage. *Small Methods* **2020**, *4*, 1900529. [CrossRef]
25. Qian, J.; Wu, C.; Cao, Y.; Ma, Z.; Huang, Y.; Ai, X.; Yang, H. Prussian blue cathode materials for sodium-ion batteries and other ion batteries. *Adv. Energy Mater.* **2018**, *8*, 1702619. [CrossRef]
26. Lee, H.W.; Wang, R.Y.; Pasta, M.; Lee, S.W.; Liu, N.; Cui, Y. Manganese hexacyanomanganate open framework as a high-capacity positive electrode material for sodium-ion batteries. *Nat. Commun.* **2014**, *5*, 5280. [CrossRef]
27. Pasta, M.; Wessells, C.D.; Liu, N.; Nelson, J.; McDowell, M.T.; Huggins, R.A.; Toney, M.F.; Cui, Y. Full open-framework batteries for stationary energy storage. *Nat. Commun.* **2014**, *5*, 3007. [CrossRef]
28. Nie, P.; Shen, L.F.; Luo, H.F.; Ding, B.; Xu, G.Y.; Wang, J.; Zhang, X.G. Prussian blue analogues: A new class of anode materials for lithium ion batteries. *J. Mater. Chem. A* **2014**, *2*, 5852–5857. [CrossRef]
29. Wheeler, S.; Capone, I.; Day, S.; Tang, C.; Pasta, M. Low-Potential Prussian blue Analogues for Sodium-Ion Batteries: Manganese Hexacyanochromate. *Chem. Mater.* **2019**, *31*, 2619–2626. [CrossRef]
30. Guo, S.H.; Yu, H.J.; Liu, D.Q.; Tian, W.; Liu, X.Z.; Hanada, N.; Ishida, M.; Zhou, H.S. A novel tunnel $Na_{0.61}Ti_{0.48}Mn_{0.52}O_2$ cathode material for sodium-ion batteries. *Chem. Commun.* **2014**, *50*, 7998–8001. [CrossRef]
31. Wang, Y.S.; Xiao, R.J.; Hu, Y.S.; Avdeev, M.; Chen, L.Q. P2-$Na_{0.6}$ [$Cr_{0.6}Ti_{0.4}$] O_2 cation-disordered electrode for high-rate symmetric rechargeable sodium-ion batteries. *Nat. Commun.* **2015**, *6*, 6954. [CrossRef] [PubMed]
32. Shanmugam, R.; Lai, W. $Na_{2/3}Ni_{1/3}Ti_{2/3}O_2$: "Bi-Functional" Electrode Materials for Na-Ion Batteries. *ECS Electrochem. Lett.* **2014**, *3*, A23–A25. [CrossRef]
33. Wang, Y.S.; Zhu, W.; Guerfi, A.; Kim, C.; Zaghib, K. Roles of Ti in Electrode Materials for Sodium-Ion Batteries. *Front. Energy Res.* **2019**, *7*, 28. [CrossRef]

34. Li, J.; Liu, J.; Sun, Q.; Banis, M.N.; Sun, X.; Sham, T.K. Tracking the effect of sodium insertion/extraction in amorphous and anatase TiO_2 nanotubes. *J. Phys. Chem. C* **2017**, *121*, 11773–11782. [CrossRef]
35. Yang, G.Z.; Song, H.W.; Wu, M.M.; Wang, C.X. Porous $NaTi_2$ $(PO_4)_3$ nanocubes: A high-rate nonaqueous sodium anode material with more than 10,000 cycle life. *J. Mater. Chem. A* **2015**, *3*, 18718–18726. [CrossRef]
36. Guo, S.H.; Yi, J.; Sun, Y.; Zhou, H.S. Recent advances in titanium-based electrode materials for stationary sodium-ion batteries. *Energy Environ. Sci.* **2016**, *9*, 2978–3006. [CrossRef]
37. Sun, X.; Ji, X.Y.; Zhou, Y.T.; Shao, Y.; Zang, Y.; Wen, Z.Y.; Chen, C.H. A new gridding cyanoferrate anode material for lithium and sodium ion batteries: $Ti_{0.75}Fe_{0.25}[Fe(CN)_6]_{0.96}{\cdot}1.9H_2O$ with excellent electrochemical properties. *J. Power Sources* **2016**, *314*, 35–38. [CrossRef]
38. Xie, M.; Huang, Y.; Xu, M.; Chen, R.; Zhang, X.; Li, L.; Wu, F. Sodium titanium hexacyanoferrate as an environmentally friendly and low-cost cathode material for sodium-ion batteries. *J. Power Sources* **2016**, *302*, 7–12. [CrossRef]
39. Luo, Y.; Shen, B.; Guo, B.; Hu, L.; Xu, Q.; Zhan, R.; Zhang, Y.; Bao, S.; Xu, M. Potassium titanium hexacyanoferrate as a cathode material for potassiumion Batteries. *J. Phys. Chem. Solids* **2018**, *122*, 31–35. [CrossRef]
40. Song, J.; Wang, L.; Lu, Y.; Liu, J.; Guo, B.; Xiao, P.; Lee, J.J.; Yang, X.Q.; Henkelman, G.; Goodenough, J.B. Removal of Interstitial H_2O in Hexacyanometallates for a Superior Cathode of a Sodium-Ion Battery. *J. Am. Chem. Soc.* **2015**, *137*, 2658. [CrossRef]
41. Kettle, S.F.A.; Diana, E.; Boccaleri, E.; Stanghellini, P.L. The Vibrational Spectra of the Cyanide Ligand Revisited. Bridging Cyanides. *Inorg. Chem.* **2007**, *46*, 7. [CrossRef] [PubMed]
42. Giorgetti, M.; Berrettoni, M.; Filipponi, A.; Kulesza, P.J.; Marassi, R. Evidence of four-body contributions in the EXAFS spectrum of $Na_2Co[Fe(CN)_6]$. *Chem. Phys. Lett.* **1997**, *275*, 108–112. [CrossRef]
43. Luca, V.; Djajanti, S.; Howe, R.F. Structural and Electronic Properties of Sol-Gel Titanium Oxides Studied by X-ray Absorption Spectroscopy. *J. Phys. Chem. B* **1998**, *102*, 10650–10657. [CrossRef]
44. Brydsoni, R.; Sauer, H.; Engel, W.; Thomas, J.M.; Zeitler, E.; Kosugi, N.; Kuroda, H. Electron energy loss and x-ray absorption spectroscopy of rutile and anatase: A test of structural sensitivity. *J. Phys. Condens. Matter* **1989**, *1*, 797–812. [CrossRef]
45. Beaurepair, E.; Lewonczu, S.; Ringeisse, J.; Parlebas, J.C.; Uozumi, T.; Okada, K.; Kotani, A. Comparison between BIS and Ti K-XAS for TiO_2: Experimental and Theoretical Study. *Europhys. Lett.* **1993**, *22*, 463–467. [CrossRef]
46. Mullaliu, A.; Conti, P.; Aquilanti, G.; Plaisier, J.R.; Stievano, L.; Giorgetti, M. Operando XAFS and XRD Study of a Prussian Blue Analogue Cathode Material: Iron Hexacyanocobaltate. *Condens. Matter* **2018**, *3*, 36. [CrossRef]
47. Krysina, O.V.; Timchenko, N.A.; Koval, N.N.; Zubavichus, Y.V. Structure of the local environment of titanium atoms in multicomponent nitride coatings produced by plasma-ion techniques. *J. Phys. Conf. Ser.* **2016**, *699*, 012060. [CrossRef]
48. Lu, Y.H.; Wang, L.; Cheng, J.G.; Goodenough, J.B. Prussian blue: A new framework of electrode materials for sodium batteries. *Chem. Commun.* **2012**, *48*, 6544. [CrossRef]
49. Rodríguez-Carvajal, J. Recent advances in magnetic structure determination by neutron powder diffraction. *Phys. B Phys. Condens. Matter* **1993**, *192*, 55–69. [CrossRef]
50. Ravel, B.; Newville, M. ATHENA, ARTEMIS, HEPHAESTUS: Data analysis for X-ray absorption spectroscopy using IFEFFIT. *J. Synchrotron Radiat.* **2005**, *12*, 537–541. [CrossRef]